Thermal Science and Engineering Progress 50 (2024) 102589

Contents lists available at ScienceDirect

Thermal Science and Engineering Progress

journal homepage: www.elsevier.com/locate/tsep

# Mixed bioconvection of nanofluid of oxytactic bacteria through a porous cavity with inlet and outlet under periodic magnetic field using artificial intelligence based on LightGBM algorithm

Shafqat Hussain [a,*], Hakan F. Öztop [b,c,d], Abdullah Madhi Alsharif [e], Fatih Ertam [f]

[a] Institut für Angewandte Mathematik (LS III), Technische Universität Dortmund, Germany
[b] Department of Mechanical and Nuclear Engineering, College of Engineering, University of Sharjah, 27272 Sharjah, United Arab Emirates
[c] Department of Mechanical Engineering, Technology Faculty, Firat University, Elazig, Turkiye
[d] Department of Medical Research, China Med. University Hospital, China Med. University, Taichung, Taiwan
[e] Department of Mathematics and Statistics, College of Science, Taif University, Saudi Arabia
[f] Department of Digital Forensics Engineering, Technology Faculty, Firat University, Elazig, Turkiye

ARTICLE INFO

*Keywords:*
square cavity
Periodic magnetic field
Hybrid nanofluid
Finite element method
Artificial intelligence
LightGBM

ABSTRACT

The comprehension of microorganisms' responses to magnetic field and fluid motion offers potential for the advancement of targeted drug delivery systems or medical interventions reliant on biological fluids. In this paper, the mixed bioconvection flow of nanofluid of oxytactic bacteria has been investigated through a porous cavity with inlet and outlet ports under the impact of periodic magnetic field. All the walls of the cavity are fixed at the constant high temperature. The proposed problem has been modeled first and then simulated using the finite element method. The computed computational fluid dynamics results have been analyzed for the several important controlling parameters. It is observed that there is at least 65% increment on heat transfer between the lowest and highest Peclet numbers. Further, regression analysis was conducted using the LightGBM algorithm. Careful parameter tuning was performed to avoid overfitting, ensuring that the model did not memorize the training data. According to the $\mathbb{R}^2$ values used for regression analysis, in the 18 datasets used for the performance metric comparison of the artificial intelligence model, a total of 18 targets were tried to be predicted for different Richardson number (0.1, 1, and 10) and Lewis Number (0.1, 1, and 10) values for each motile microorganisms, temperature and oxygen concentration values specified in the datasets, and a minimum accuracy of 95% and a maximum accuracy of 98% were obtained. These findings demonstrate the capability of the LightGBM algorithm to accurately predict the target variable within a high range of accuracy for the given datasets.

## 1. Introduction

The term "bioconvection" represents the macroscopic convection in the fluid generated by the density gradient setup by directional collective swimming of microorganisms under the effect of light, gravity, or chemical reaction (oxygen) [1,2]. Based on cause of impellent, these motile microorganism can be divided in different categories such as chemotactic, gravitactic, gyrotactic, oxytactic, thermotactic and phototactic. Such motile microorganisms clustered near the top surface of the fluid and makes the upper surface as dense which is then becomes unstable or destabilized. Consequently, the macroscopic convection develops due to the crumbling of upward swimming. The bioconvection has extensive application, for example in bio-microsystems and micro heat cylinders, including micro-reactors for biotechnology for mass transportation, microbial enhanced oil recovery, biosensors and biotechnology, bio-machines, enzyme biosensors, etc., [1,3]. Platt [4] was the first who introduced the phenomenon of bioconvection and afterwards, numerous works have been considered including the boundary conditions, different geometries, bioconvection patterns, and the presence of different microorganisms, [3,5–8].

The heat transfer characteristics can be improvement by improving the thermal conductivity of the fluid. To this end, one of the way is to insert the nano-sized particles into the conventional fluids such as water, ethylene glycol and oils. Choi [9] proposed this idea in 1995 and enhanced the thermal conductivity of fluids with nanoparticles. Nanofluids are engineered suspensions of nanoparticles (typically metallic or non-metallic) dispersed within a base fluid (such

* Corresponding author.
*E-mail address:* shafqat.hussain@math.tu-dortmund.de (S. Hussain).

https://doi.org/10.1016/j.tsep.2024.102589
Received 19 December 2023; Received in revised form 7 April 2024; Accepted 21 April 2024
Available online 24 April 2024

**Nomenclature**

| | |
|---|---|
| $C_p$ | Specific heat (J kg$^{-1}$ K$^{-1}$) |
| $C$ | Oxygen concentration |
| $D_c$ | Oxygen diffusivity (m$^2$ s$^{-1}$) |
| $D_n$ | Microorganisms diffusivity (m$^2$ s$^{-1}$) |
| $g$ | Gravitational acceleration (m s$^{-2}$) |
| $H$ | Cavity dimension (m) |
| $Ha$ | Hartmann number |
| $k$ | Thermal conductivity (W m$^{-1}$ K$^{-1}$) |
| $Le$ | Lewis number |
| $m$ | Motile microorganisms (dimensional) |
| $m_0$ | The reference density number |
| $N$ | Motile microorganisms density |
| $Nn$ | Density of the motile microorganisms number |
| $Nu_{\text{avg}}$ | Nusselt number (average) |
| $Pr$ | Prandtl number |
| $p$ | Pressure (N m$^{-2}$) |
| $Pe$ | Peclet number |
| $Ra$ | Rayleigh number |
| $Rb$ | Bioconvection Rayleigh number |
| $Sh$ | Sherwood number |
| $Sc$ | Schmidt number |
| $Sh_{\text{avg}}$ | Sherwood number (average) |
| $u_0$ | Initial velocity |
| $T$ | Temperature (K) |
| $u, v$ | Velocities (m s$^{-1}$) |
| $X, Y$ | Dimensionless Cartesian coordinates |
| $x, y$ | Cartesian coordinates (m) |
| **Greek symbols** | |
| $\alpha$ | Thermal-diffusivity (m$^2$ s$^{-1}$) |
| $\beta$ | Thermal expansion coefficient (K$^{-1}$) |
| $\theta$ | Inclination angle of magnetic field |
| $\mu$ | Dynamic-viscosity (kg m$^{-1}$ s$^{-1}$) |
| $\nu$ | Kinematic-viscosity (m$^2$ s$^{-1}$) |
| $\xi$ | Oxygen concentration |
| $\rho$ | Density (kg m$^{-3}$) |
| $\phi$ | Nanoparticles concentration |
| $\psi$ | Stream function |
| **Subscripts** | |
| avg | Average |
| $c$ | Cold |
| $f$ | Water properties |
| $h$ | Hot |
| $hnf$ | Hybrid nanofluid |
| $p$ | Nanoparticles |
| $w$ | Wall |

as water, oil, or ethylene glycol). They exhibit enhanced thermophysical properties compared to traditional fluids due to the presence of nanoparticles. The physical mechanisms behind the effects of nanofluids involve considerations of thermal conductivity, fluid dynamics, and nanoparticle dispersion stability. Nanoparticles have a much higher surface area-to-volume ratio compared to larger particles. This increased surface area allows for more interactions with the surrounding fluid molecules, leading to enhanced thermal conductivity. Brownian motion of nanoparticles within the fluid also contributes to enhanced thermal conductivity by facilitating better heat transfer between the nanoparticles and the base fluid. The addition of nanoparticles alters the flow behavior of the nanofluid. The presence of nanoparticles can affect the viscosity and density of the fluid, impacting its flow characteristics. The stability of nanoparticles within the base fluid is crucial for maintaining the enhanced properties of nanofluids over time. Agglomeration or settling of nanoparticles can reduce their effectiveness. Thus, the physical mechanisms behind the effects of nanofluids involve intricate interplays between thermal conductivity enhancement, fluid dynamics alterations, and nanoparticle dispersion stability. Understanding and optimizing these mechanisms are essential for harnessing the full potential of nanofluids in various applications, including heat transfer enhancement in cooling systems, thermal management in electronics, and solar energy conversion. The concept of nanofluid bioconvection was introduced by Kuznetsov [10]. Sheremet et al. [11] explored the MHD-free convection flow nanofluids and gyrotactic microorganism in an inclined square space. It was observed that Hartmann number ($Ha$) leads to a reduction in the heat and mass transfers. Mandal et al. [12] investigated the MHD mixed bioconvection of the copper–water nanofluid in the presence of oxytactic microorganisms in a cavity with the wavy wall. It was observed that undulating curved surface enhances the heat transfers up to certain optimal magnitudes of undulations ($n$). Some studies related to nanofluid can be found in [13–16].

Problems involving porous medium have also attracted a great deal of attention due to many applications, such as food industry, geothermal energy systems, chemical catalytic convertors, etc. The existence of microorganisms in the nanofluids with the porous medium gains the attention of researches due to its important application in bio-nano-technology. Balla et al. [17] analyzed the bioconvection flow of oxytactic microorganism and nanofluids in a porous square enclosure. They concluded that the mean Nusselt number was augmented by the Lewis number, Peclet number, Brownian motion, and thermal force.

Regression analysis is a sub-branch of machine learning and aims to model the relationship of a dependent variable with one or more independent variables. The dependent variable takes a continuous or numerical value while the independent variables can be measurable or categorical. The main goal of regression analysis can be expressed as the estimation of the dependent variable with the given values of the independent variables. These estimates can be used to predict future values or unknown values based on available data. Regression analysis attempts to realize these predictions by constructing a regression model [18,19]. Regression analysis is frequently used in the estimation of simulation data obtained in the CFD field with artificial intelligence. Its main purpose is to model how a dependent variable depends on one or more independent variables. This modeling process is used when the dependent variable must take a continuous value.

Gradient Boosting Decision Trees (GBDT) is a powerful machine learning technique that combines the principles of gradient boosting and decision trees. Gradient Boosting Decision Trees (GBDT) is a widely used artificial intelligence technique for classification and regression problems. Its main goal is to build a powerful prediction model by combining decision trees that are weak learners It is widely used for both regression and classification tasks due to its ability to handle complex data patterns and produce accurate predictions [20]. In GBDT, decision trees are sequentially trained, with each subsequent tree learning from the mistakes or residuals of the previous trees. The process involves iteratively minimizing a loss function by adding new trees that complement the previous ones. This iterative process improves the overall prediction accuracy by focusing on the instances that are more difficult to predict [21]. In their study on room temperature, Lin et al. [22] utilized the LightGBM algorithm. Through numerous numerical simulations, they demonstrated that thermal models based on both XGBoost and LightGBM outperformed other machine learning models in both steady-state and transient scenarios. They showed that the root mean square error (RMSE) of the temperature prediction was less than 1.0 °C.

In their study, Yao et al. [23] employed the LightGBM algorithm. In their a priori study, the authors employed the LightGBM algorithm to train Gradient Boosting Decision Trees (GBDTs) on time series data of different self-igniting mixtures. Specifically, they used LightGBM to predict the species compositions and thermodynamic states at the

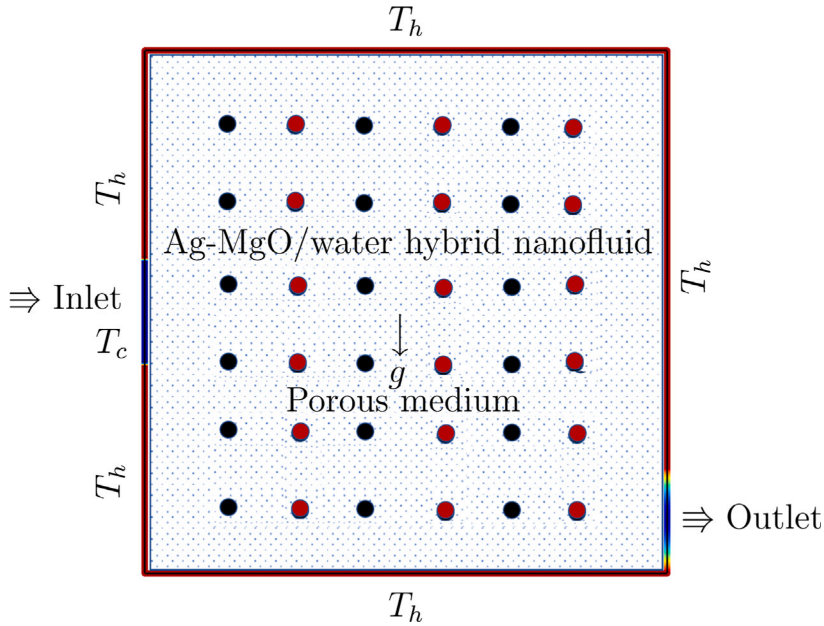


**Fig. 1.** The problem configuration.

subsequent time step from the time of ignition to equilibrium composition. The GBDT model exhibited reasonable predictions, indicating its effectiveness in capturing the dynamics of the system. In the studies conducted with XBBoost and LightGBM algorithms among the GBDT algorithms, the default parameters of the algorithm used are generally used. The use of such algorithms with their default parameters may lead to overfitting. The parameters were adjusted in the study to avoid overfitting. In addition, in this study, it was aimed to use only 70% of the training data and not to use too much of the total data. Thus, more data (30%) was used for the test data.

In light of the above-mentioned literature survey, it can be observed that the bioconvection of nanofluid inside various configurations have been investigated mostly for the natural convection, however, there are a few studies considering the mixed bioconvection flow of nanofluid under the impact of magnetic field. Therefore, the aim of the present work is to explore the mixed bioconvection flow of nanofluid of oxytactic bacteria through a porous cavity with inlet and outlet ports under the impact of periodic magnetic field. The governing system of dimensionless equations have been solved using the higher order finite element method. The machine learning approach based on the LightGBM algorithm has also been utilized to predict the quantities of interest from the data set. Finally, The obtained numerical outcomes will be presented and discussed in detail. To the best of authors' knowledge, mixed bioconvection flow of nanofluid has not been investigated in the proposed cavity configuration in case of inclined periodic magnetic field. The obtained results can find various applications for example, design of bio-energy systems, efficient working of heat exchangers, cooling of microelectronics, drug delivery systems or medical interventions, fuel cells, etc.

## 2. Model of the problem

The problem being considered here consists of a two-dimensional, incompressible, laminar, steady bioconvection of hybrid nanofluid flow in a square cavity with inlet and outlet ports as depicted in Fig. 1. All the cavity walls are subjected to the hot walls at temperature $T_h$. Bacteria's swimming velocity and direction are not affected by nanoparticles in order not to permit for bioconvection instability. Further, bacteria do not eat porous matter and size of bacteria is smaller than pores. Moreover, the nanoparticles are suspended stable. A periodic-magnetic field is imposed at an angle of $\theta$. The porous medium is assumed to be homogeneous, isotropic and in thermal equilibrium with base fluid. The Boussinesq approximations are considered for the variation of density, Further, viscous dissipation, Joule dissipation, radiative heat transfer and induced magnetic field are not taken into consideration. The thermal and electrical characteristics of the base fluid and nanoparticles are mentioned in Table 1.

**Table 1**
Thermophysical and electrical properties of water and nanoparticles [24].

| Property | H2O | Ag | MgO |
|---|---|---|---|
| $\rho\,(\mathrm{kg/m^3})$ | 997.1 | 10 500 | 3580 |
| $k\,(\mathrm{W/m\,K})$ | 0.613 | 429 | 30 |
| $C_p\,(\mathrm{J/kg\,K})$ | 4179 | 235 | 879 |
| $\beta\,(1/\mathrm{K})$ | $21\times10^{-5}$ | $5.4\times10^{-5}$ | $33.6\times10^{-6}$ |
| $\sigma\,(\Omega^{-1}\,\mathrm{m}^{-1})$ | 0.05 | $6.3\times10^{7}$ | $1.42\times10^{-3}$ |

The corresponding correlations for the thermophysical and electrical properties are utilized from [2].

The proposed problem is modeled as mass conservation, momentum conservation, energy conservation, as follows [2,25]

$$\frac{\partial u}{\partial x}+\frac{\partial v}{\partial y}=0 \tag{1a}$$

$$\begin{aligned}\frac{\mu_{hf}}{\epsilon}\nabla^2 u=&\frac{\partial p}{\partial x}+\frac{\rho_{hf}}{\epsilon^2}\left(u\frac{\partial u}{\partial x}+v\frac{\partial u}{\partial y}\right)+\frac{\mu_{hf}}{K}u+\frac{\rho_{hf}C_f}{\sqrt{K}}u\sqrt{u^2+v^2}\\&-\sigma_{hf}B_0^2\sin^2\left(\frac{\pi}{\lambda}(y\cos\theta-x\sin\theta)\right)\left[v\sin\theta\cos\theta-u\sin^2\theta\right]\end{aligned} \tag{1b}$$

$$\begin{aligned}\frac{\mu_{hf}}{\epsilon}\nabla^2 v=&\frac{\partial p}{\partial y}+\frac{\rho_{hf}}{\epsilon^2}\left(u\frac{\partial v}{\partial x}+v\frac{\partial v}{\partial y}\right)+\frac{\mu_{hf}}{K}v+\frac{\rho_{hf}C_f}{\sqrt{K}}v\sqrt{u^2+v^2}\\&-\sigma_{hf}B_0^2\sin^2\left(\frac{\pi}{\lambda}(y\cos\theta-x\sin\theta)\right)\left[u\sin\theta\cos\theta-v\cos^2\theta\right]\\&-(\gamma\Delta\rho\cdot m-(\rho\beta)_{hf}(T-T_c))g\end{aligned} \tag{1c}$$

$$\alpha_{hf}\nabla^2 T=u\frac{\partial T}{\partial x}+v\frac{\partial T}{\partial y} \tag{1d}$$

$$D_c\nabla^2 C=u\frac{\partial C}{\partial x}+v\frac{\partial C}{\partial y}+\delta m \tag{1e}$$

$$\frac{\partial}{\partial x}\left[um+\tilde{u}m-D_n\frac{\partial m}{\partial x}\right]+\frac{\partial}{\partial y}\left[vm+\tilde{v}m-D_n\frac{\partial m}{\partial y}\right]=0, \tag{1f}$$

The following non-dimensional variables are introduced to convert the dimensional equations into dimensionless form (1)

$$x' = \frac{x}{H},\ u' = \frac{u}{u_0},\ y' = \frac{y}{H},\ v' = \frac{v}{u_0},\ P' = \frac{p}{\rho u_0^2},$$
$$T' = \frac{T - T_c}{T_h - T_c},\ \xi = \frac{C - C_{\min}}{\Delta C},\ N = \frac{m}{m_0}, \tag{2}$$

where $m_0$ representing the number density of microorganisms. The prime notation is dropped after substituting the new variables into the dimensional equations. The dimensionless form of the equations is then becomes as follows [25]

$$\frac{\partial u}{\partial x} + \frac{\partial v}{\partial y} = 0 \tag{3a}$$

$$\frac{1}{\epsilon Re}\frac{\nu_{hf}}{\nu_f}\nabla^2 u = \frac{\partial P}{\partial x} + \frac{1}{\epsilon^2}\left(u\frac{\partial u}{\partial x} + v\frac{\partial u}{\partial y}\right) + \left(\frac{\nu_{hf}}{\nu_f}\frac{1}{DaRe} + \frac{C_f\sqrt{u^2+v^2}}{\sqrt{Da}}\right)u \tag{3b}$$
$$- \frac{\rho_f}{\rho_{hf}}\frac{\sigma_{hf}}{\sigma_f}\frac{Ha^2}{Re}\sin^2\left(\frac{\pi}{\Lambda}(y\cos\theta - x\sin\theta)\right)\left[v\sin\theta\cos\theta - u\sin^2\theta\right]$$

$$\frac{1}{\epsilon Re}\frac{\nu_{hf}}{\nu_f}\nabla^2 v = \frac{\partial P}{\partial y} + \frac{1}{\epsilon^2}\left(u\frac{\partial v}{\partial x} + v\frac{\partial v}{\partial y}\right) + \left(\frac{\nu_{hf}}{\nu_f}\frac{1}{DaRe} + \frac{C_f\sqrt{u^2+v^2}}{\sqrt{Da}}\right)v \tag{3c}$$
$$- \frac{\rho_f}{\rho_{hf}}\frac{\sigma_{hf}}{\sigma_f}\frac{Ha^2}{Re}\sin^2\left(\frac{\pi}{\Lambda}(y\cos\theta - x\sin\theta)\right)\left[u\sin\theta\cos\theta - v\cos^2\theta\right]$$
$$- \frac{(\rho\beta)_{hf}}{\rho_{hf}\beta_f}\frac{Gr}{Re^2}(T - R_b N)$$

$$\frac{1}{PrRe}\frac{\alpha_{hf}}{\alpha_f}\nabla^2 T = u\frac{\partial T}{\partial x} + v\frac{\partial T}{\partial y} \tag{3d}$$

$$\frac{1}{PrReLe}\nabla^2\xi = u\frac{\partial \xi}{\partial x} + v\frac{\partial \xi}{\partial y} + \frac{\zeta}{PrReLe}N \tag{3e}$$

$$\frac{1}{PrReLe}\nabla^2 N = \chi\left(u\frac{\partial N}{\partial x} + v\frac{\partial N}{\partial y}\right) + \frac{Pe}{PrReLe}$$
$$\times\left(N\frac{\partial^2\xi}{\partial x^2} + N\frac{\partial^2\xi}{\partial y^2} + \frac{\partial N}{\partial x}\frac{\partial \xi}{\partial x} + \frac{\partial N}{\partial y}\frac{\partial \xi}{\partial y}\right), \tag{3f}$$

where $\zeta = (m_0\delta L^2/(D_c\Delta C))$ denotes the oxygen consumption, $\Lambda$ represents the dimensionless period of magnetic field, $\chi = D_c/D_n$ stands for the diffusion ratio.

The following dimensionless parameters are involved in the above equations

$$Pr = \frac{\nu_f}{\alpha_f},\ Re = \frac{u_0 H}{\nu_f},\ Gr = \frac{g\beta_f H^3(T_h - T_c)}{\nu_f^2},$$
$$Ri = \frac{Gr}{Re^2},\ R_b = \frac{m_0(\rho_{cell} - \rho_f)\gamma}{\rho_f\beta_f(T_h - T_c)} \tag{4}$$
$$Ha = B_0 H\sqrt{\frac{\sigma_f}{\mu_f}},\ Pe = \frac{bW_c}{D_n},\ Le = \frac{\alpha_f}{D_c},\ Da = \frac{K}{H^2}, \tag{5}$$

The boundary conditions for the governing equations may be expressed as

at the inlet port: $u = 1,\ v = 0,\ T = 0,\ \xi = N = 0$

on the outlet port: $\frac{\partial u}{\partial x} = \frac{\partial v}{\partial x} = \frac{\partial T}{\partial y} = \frac{\partial \xi}{\partial y} = \frac{\partial N}{\partial y} = 0$

on the bottom wall: $u = v = 0,\ -\frac{\partial T}{\partial y} = 0,\ \xi = 1,\ PeN\frac{\partial \xi}{\partial y} = \frac{\partial N}{\partial y}$

on all the other walls: $u = v = 0,\ T = \xi = N = 1.$

## 3. The Nusselt number ($Nu$), Sherwood number oxygen ($Sh$) and density of motile microorganisms ($Nn$)

The corresponding quantities of interest, namely, local and average Nusselt number, Sherwood number of oxygen and density of motile microorganisms. These quantities at the local level are defined as

$$Nu_{\text{loc}} = -\frac{k_{hnf}}{k_f}\frac{\partial T}{\partial \mathbf{n}},\quad Sh_{\text{loc}} = -\frac{\partial \xi}{\partial \mathbf{n}},\quad Nn_{\text{loc}} = -\frac{\partial N}{\partial \mathbf{n}}, \tag{6}$$

where $\mathbf{n}$ depicts the normal vector to the boundary wall. In order to obtain the average quantities, each of the above is integrated over the heated section

$$Nu_{\text{avg,i}} = \int_0^S Nu_{\text{loc}}\,dS,\quad Sh_{\text{avg,i}} = \int_0^S Sh_{\text{loc}}\,dS,$$
$$Nn_{\text{avg,i}} = \int_0^S Sh_{\text{loc}}\,dS, \tag{7}$$

where $i$ denotes l, r, t and b which corresponds to the left, right, top and bottom walls, respectively, and $S$ is the length of the heated wall. Since all the cavity walls are subjected to the heat transfer, the total Nusselt number can be obtained by summing up the individual wall average Nusselt numbers [26]. Thus, the total Nusselt number of the cavity becomes

$$Nu_{\text{avg}} = \frac{1}{4}\sum_i Nu_{\text{avg,i}},\quad Sh_{\text{avg}} = \frac{1}{4}\sum_i Sh_{\text{avg,i}},\quad Nn_{\text{avg}} = \frac{1}{4}\sum_i Sh_{\text{avg,i}}. \tag{8}$$

**Table 2**
The average Nusselt number for present and Gibanov et al. [30].

| Present study | Gibanov et al. [30] |
|---|---|
| 12.57879 | 12.5335 |

## 4. Numerical methodologies

### 4.1. The finite element method

The Galerkin based finite element method has been implemented for the solution of dimensionless governing system of PDEs (3) subject to the given boundary conditions. First, a weak formulation has been achieved by multiplying the reduced system of governing equations to the appropriate test functions. Then, the finite element discretization is performed using a trial function space consisting of piecewise cubic polynomials ($\mathbb{P}_3$) for the velocity, temperature, oxygen and microorganism concentration variables. For the approximation of pressure, a space of quadratic polynomials ($\mathbb{P}_2$) is utilized. In this way, for each element, the chosen FEM pair ($\mathbb{P}_3/\mathbb{P}_2$) appends 10 unknowns in the global system matrix for each of $u, v, T, \xi, N$ components and 6 unknowns for the discrete pressure $P$. Thus, a total of 56 degrees of freedoms (DOFs) are assembled in the global system per element. The discrete system of nonlinear equations has been handled with the help of adaptive Newtons method. The linear system of equations in each nonlinear sweep, has been solved using the Gaussian elimination method. The nonlinear outer loop is terminated when the nonlinear residual drops down by $10^{-6}$ and the last iteration is accepted as the approximate solution. The solution procedure has already been employed and explained in our earlier work, see for example, [27,28] for details.

#### 4.1.1. The code validation

The FEM code has been validated in [29] for both the numerical and experimental published data. In order to strengthen the performance of the present code, the designed FEM code has been validated against the obtained results of Gibanov et al. [30] for similar configuration. An important quantity of interest, the average Nusselt number has been calculated and compared in Table 2 for $Da = 10^{-3}, Ri = 1, Pr = 6.26, \epsilon = 0.398, Re = 100, \Lambda = A = 1.2042, S1 = S2 = 0.75L, \delta = H/L = 0.3.$. The presented comparison has been found in very good agreement. To test the visual performance of the designed code, the streamlines and isotherms are plotted and demonstrated in Fig. 2.

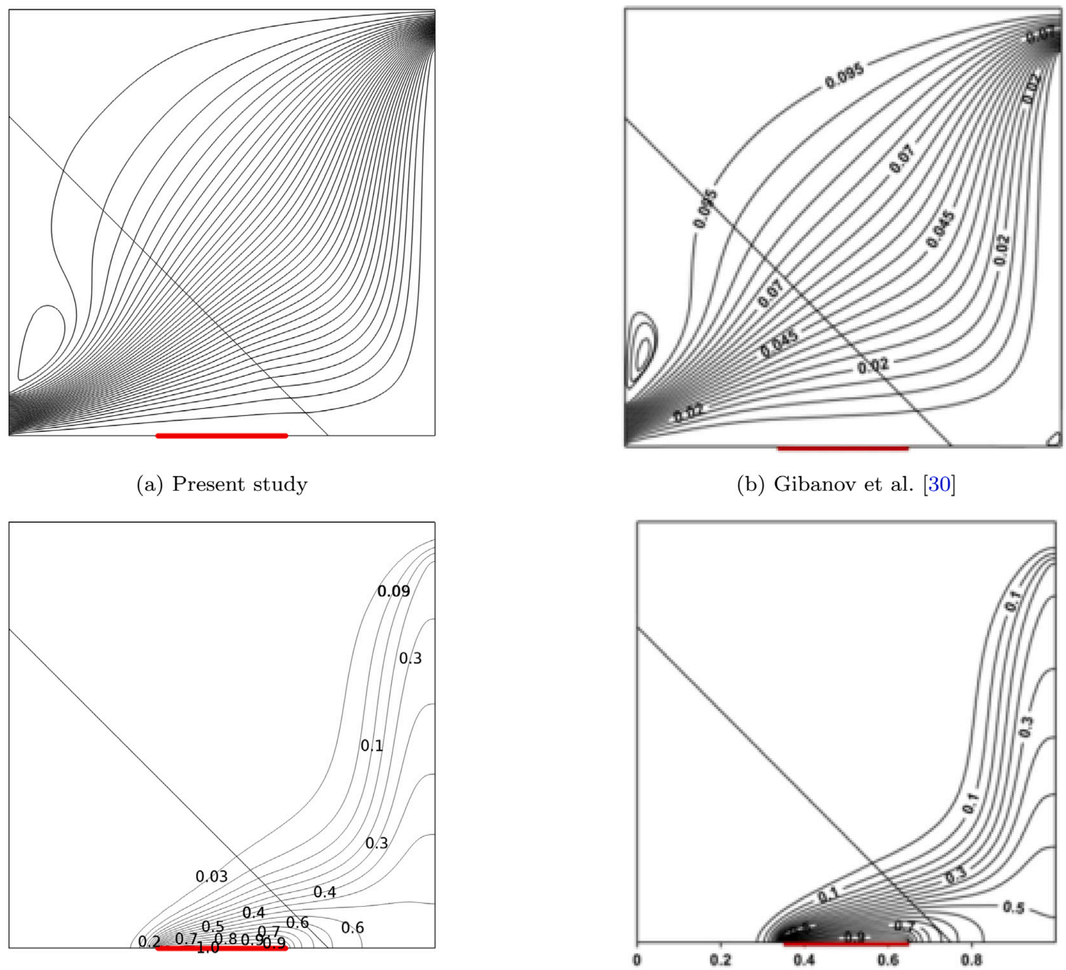


(a) Present study
(b) Gibanov et al. [30]
(c) Present study
(d) Gibanov et al. [30]

**Fig. 2.** The streamlines (above) and isotherms (below) from present study and Gibanov et al. [30] for $Da = 10^{-3}, Ri = 1, Pr = 6.26, \epsilon = 0.398, Re = 100, \Lambda = A = 1.2042, S1 = S2 = 0.75L, \delta = H/L = 0.3$.

**Table 3**
The code validation for the average Nusselt number.

| $Ra$ | $R_b$ | $Le$ | $Pe$ | $Nu_{avg}\vert_{x=0}$ | | $Nu_{avg}\vert_{x=1}$ | | $Sh_{avg}\vert_{x=0}$ | | $Sh_{avg}\vert_{x=1}$ | |
|---|---|---|---|---|---|---|---|---|---|---|---|
| | | | | Current | [8] | Current | [8] | Current | [8] | Current | [8] |
| 10 | 10 | 1 | 0.1 | 1.0774 | 1.0775 | 1.0774 | 1.0775 | 0.3368 | 0.3368 | 0.3896 | 0.3897 |
| | | | 1 | 1.0720 | 1.0720 | 1.0721 | 1.0723 | 0.3295 | 0.3296 | 0.3806 | 0.3807 |
| | | 10 | 0.1 | 1.0771 | 1.0771 | 1.0771 | 1.0771 | 0.2556 | 0.2556 | 0.4677 | 0.4677 |
| | | | 1 | 1.0396 | 1.0397 | 1.0397 | 1.0396 | 0.2298 | 0.2298 | 0.5419 | 0.5417 |
| | 100 | 1 | 0.1 | 1.0716 | 1.0717 | 1.0717 | 1.0720 | 0.3446 | 0.3447 | 0.4017 | 0.4018 |
| | | | 1 | 1.1725 | 1.1723 | 1.1731 | 1.1726 | 0.3450 | 0.3450 | 0.4061 | 0.4061 |
| 100 | 10 | 1 | 0.1 | 3.0915 | 3.0910 | 3.0921 | 3.0910 | 0.2504 | 0.2506 | 0.4723 | 0.4723 |
| | | | 1 | 2.6560 | 2.6560 | 2.6613 | 2.6559 | 0.2269 | 0.2270 | 0.5188 | 0.5183 |

### *4.1.2. The grid convergence*

To test the authenticity of the utilized code for the thermo-bioconvection of oxytactic microorganisms, the results have been demonstrated and compared in Table 3 against the results of [8]. An excellent agreement was observed between the present and reported study [8] in terms of Nusselt number.

The grid sensitivity check has been carried out for the global quantities of interest in Table 4 for fixed parameters values of $\phi = 0.01, \epsilon = 0.8, Pr = 6.2, Ha = 25, Da = 10^{-3}, \Lambda = 1, \chi = \zeta = 1, \theta = 0, Ri = Pe = 1, Le = 1,$ and $R_b = 10$. One can notice from the table that insignificant variations can be seen for the finest two grid levels of $\ell = 8, 9$. Hence, the simulations are conducted at $\ell = 8$.

### *4.2. The lightgbm algorithm*

LightGBM (Light Gradient Boosting Machine) is a novel GBDT (Gradient Boosting Decision Tree) algorithm, proposed by Ke et al. [31] in 2017, that has been used in various data mining tasks, including classification, regression, and ranking [21]. The LightGBM algorithm incorporates two innovative techniques, namely gradient-based one-side sampling and exclusive feature bundling [32]:

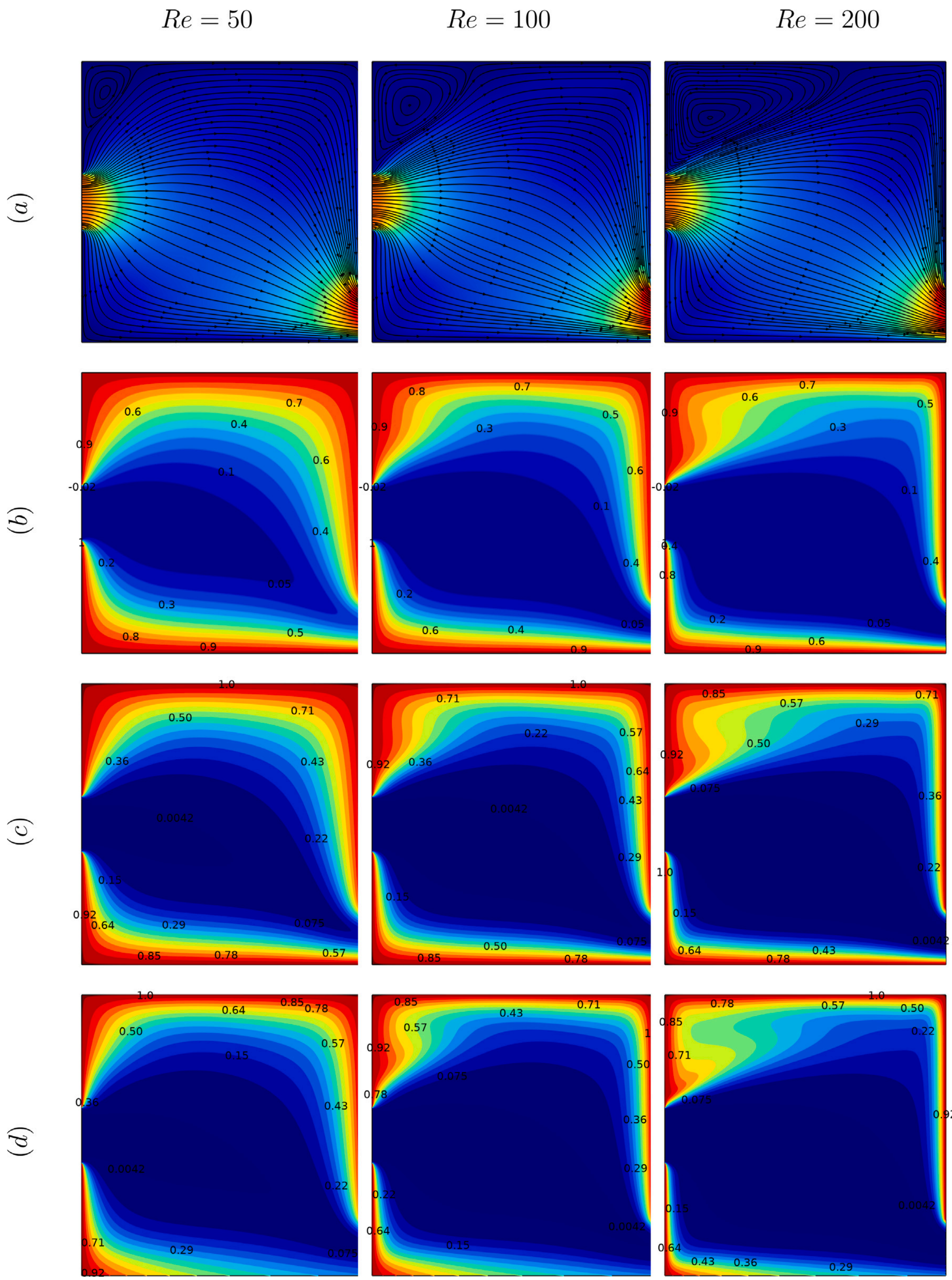


**Fig. 3.** The (a) streamlines, (b) temperature, (c) oxygen concentration, (d) motile microorganisms, for the variations of *Re*.

Gradient-based One-Side Sampling; LightGBM utilizes the gradient-based one-side sampling technique, which is an efficient sampling strategy. This technique randomly samples from the larger classes of the dataset to achieve faster training times and addresses the class imbalance problem.

Exclusive Feature Bundling; LightGBM supports exclusive feature bundling, which groups similar features together to improve memory and computational efficiency. This technique enhances overall performance while speeding up data access. Some advantages of LightGBM can be summarized as follows:

- Speed and Efficiency: LightGBM is faster than other GBDT implementations. Optimizations such as gradient-based one-side sampling and feature bundling significantly reduce training times.

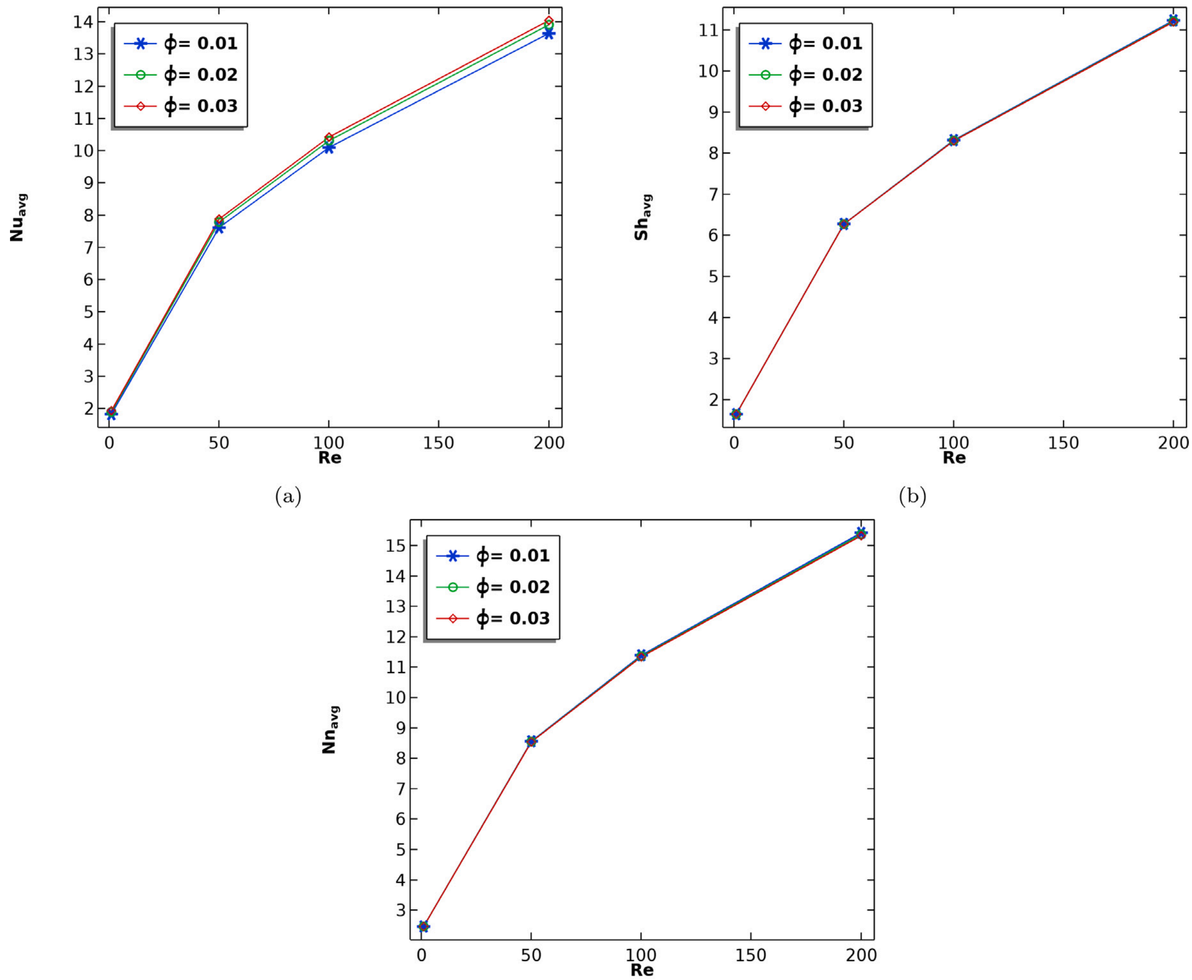


(a) (b) (c)

**Fig. 4.** The (a) average Nusselt number, (b) average Sherwood numbers and (c) average motile microorganism for the variation of $\phi$ as a function of $Re$.

**Table 4**
The grid sensitivity results for the proposed problem.

| $\ell$ | $Nu_{avg}$ | $Sh_{avg}$ | $Nn_{avg}$ |
|---|---|---|---|
| 1 | 7.1794 | 4.8683 | 5.7568 |
| 2 | 7.5664 | 5.7224 | 7.0792 |
| 3 | 8.0272 | 6.2538 | 7.9056 |
| 4 | 8.5770 | 6.8799 | 8.9285 |
| 5 | 8.9257 | 7.2309 | 9.5134 |
| 6 | 9.1431 | 7.4538 | 9.8885 |
| 7 | 9.7417 | 8.0082 | 10.8520 |
| 8 | 10.0924 | 8.3126 | 11.3840 |
| 9 | 10.0950 | 8.3127 | 11.3860 |

- Lower Memory Usage: LightGBM can handle large datasets with low memory consumption. This feature is beneficial for applications with memory constraints.
- High Prediction Performance: LightGBM provides high accuracy and generally outperforms other GBDT methods in terms of prediction performance. This is crucial for various data mining tasks, including classification, regression, and ranking. LightGBM, unlike the traditional level-wise growth strategy, utilizes a leaf-wise (leaf-based) growth strategy. This strategy increases the depth of the tree by selecting the best split downward, resulting in better prediction performance.

Also, LightGBM supports L1 and L2 regularization techniques. These techniques help mitigate overfitting and improve the generalization capability of the models. In this study, the LightGBM algorithm is used for regression analysis and a brief description of the algorithm is presented in this section. In the subsections, the datasets obtained and the performance metrics used to measure the performance of the regression analysis are mentioned.

#### 4.2.1. The datasets

For the study, a total of 18 datasets obtained from the Computational Fluid Dynamics (CFD) study were utilized. These datasets consisted of 9 sets each for $N, T$, and $\xi$ values corresponding to different $Ri$ values (0.1, 1, and 10), as well as 9 sets for $N, T$, and $\xi$ values corresponding to different $Le$ values (0.1, 1, and 10). From each dataset, 1000 data points were selected, resulting in a total of 1000 data points per set, and these data points were used for estimation purposes. Each dataset has 3 features: $x$, $y$ and class. A server computer equipped with an Intel Xenon CPU E5-260 processor and 160 GB of RAM was utilized for data processing. The data analysis was performed using Python 3 software.

#### 4.2.2. Model performance evaluation metrics

R-squared ($R^2$), Mean square error (MSE), Root Mean square error (RMSE) were used to assess the performance of the regression analysis estimation. Furthermore, the mean of the actual values (MAV) and the mean of the predicted values (MPV) were computed and compared. In the following equations, $X_i$ represents the predicted $i$th value, while the element $Y_i$ represents the actual $i$th value. The regression method

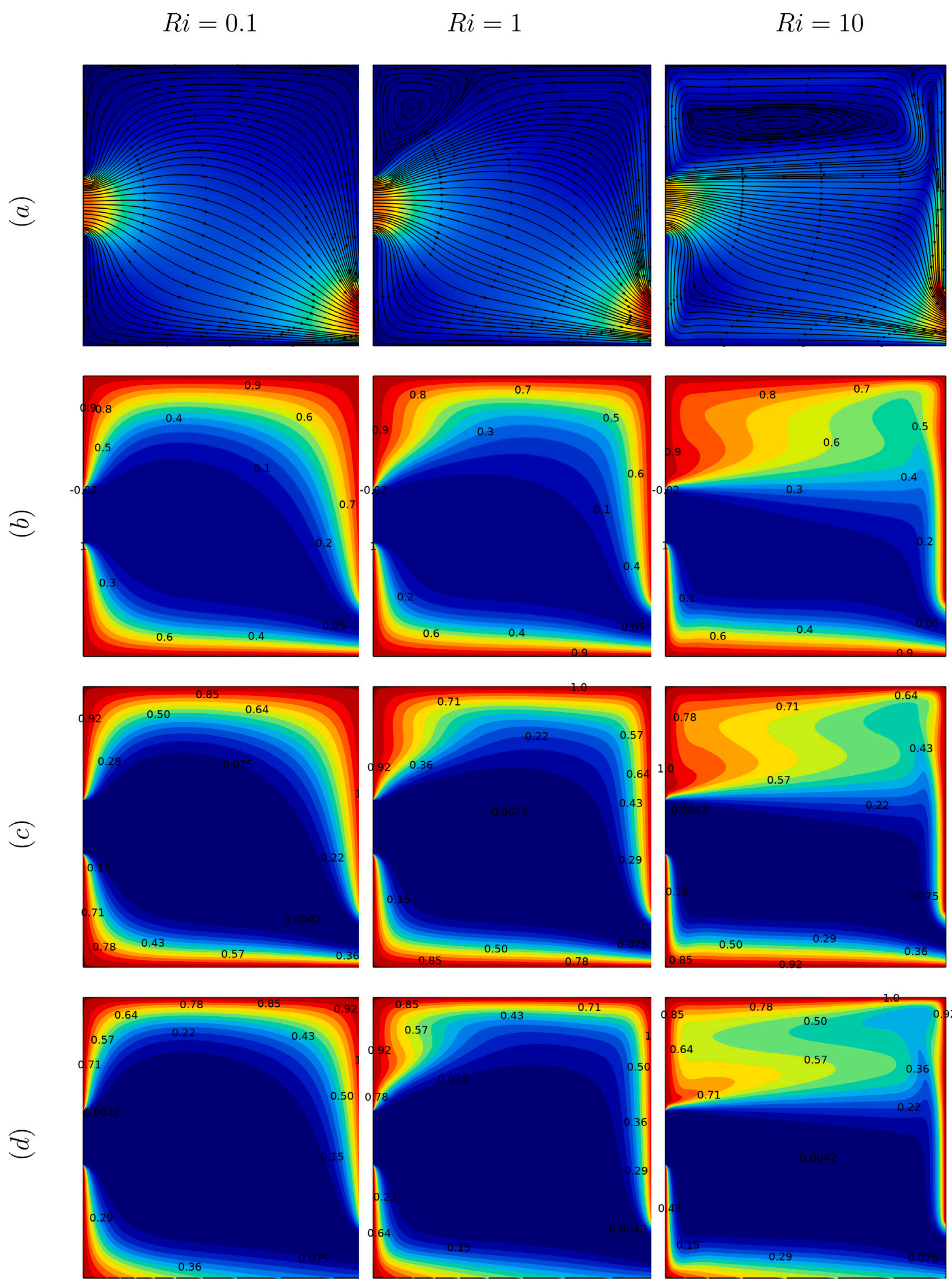


**Fig. 5.** The (a) streamlines, (b) temperature, (c) oxygen concentration, (d) motile microorganisms, for the variations of $Ri$.

predicts the $X_i$ element corresponding to the $Y_i$ element from the ground truth dataset [33]. In Eq. (9), the average of the actual values is calculated, where n represents the total number of data points.

$$Y = \frac{1}{n}\sum_{i=1}^{n} Y_i \tag{9}$$

The calculation of the R-squared ($R^2$) value is demonstrated in Eq. (10). A value close to 1 indicates that the estimation results are in good agreement with the actual values.

$$R^2 = 1 - \frac{\sum_{i=1}^{n}(X_i - Y_i)^2}{\sum_{i=1}^{n}(\bar{Y} - Y_i)^2} \tag{10}$$

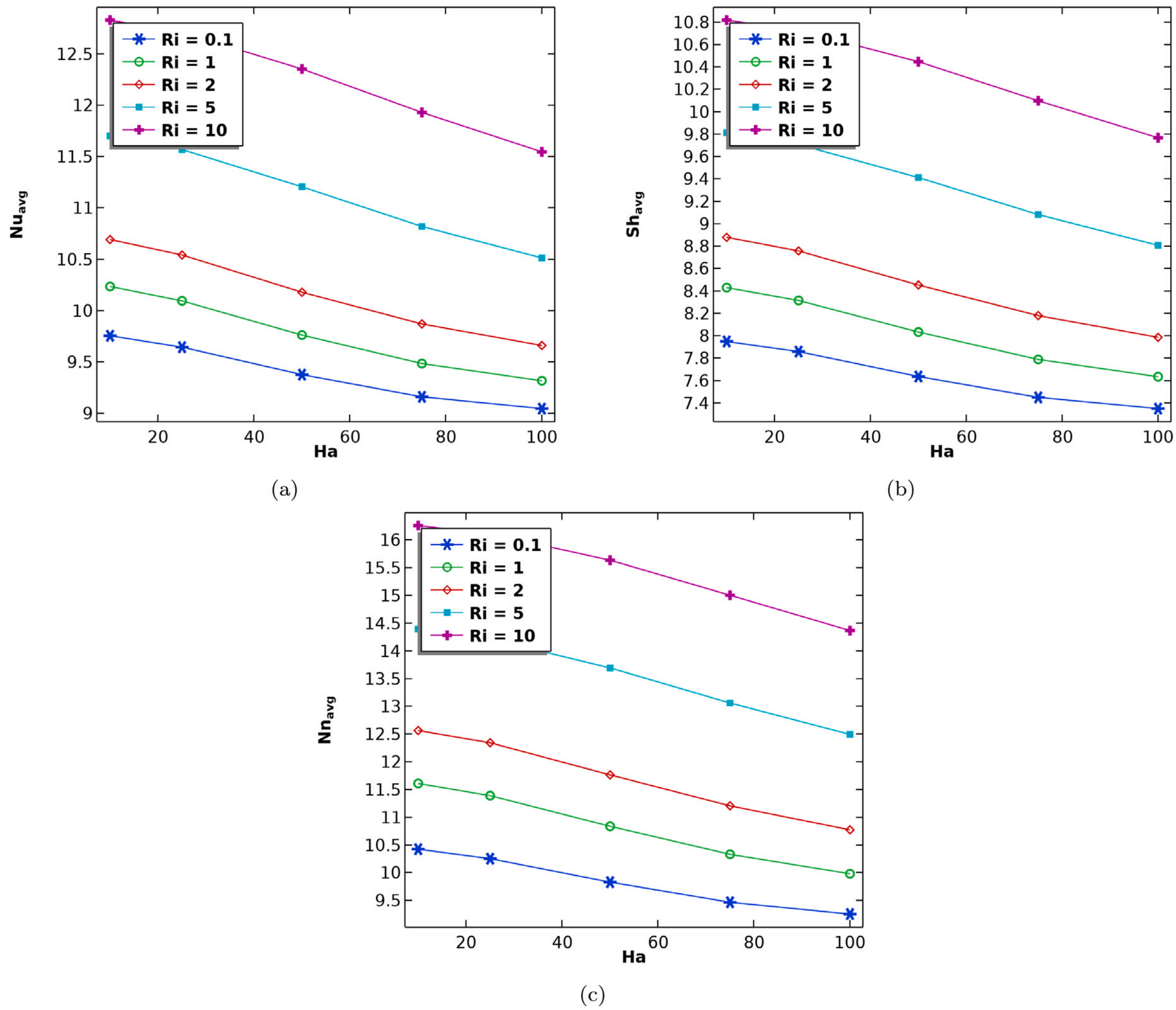


**Fig. 6.** The (a) average Nusselt number, (b) average Sherwood numbers and (c) average motile microorganism for the variation of $Ri$ as a function of $Ha$.

The Mean Squared Error (MSE) is calculated as shown in Eq. (11). A smaller MSE value indicates that the estimation results are closer to the actual values, indicating better performance. The Root Mean Squared Error (RMSE) value, given by taking the square root of MSE as shown in Eq. (12), provides a measure of the average magnitude of the estimation errors. A lower RMSE value signifies better accuracy in the estimation results [18,19].

$$\mathrm{MSE} = \frac{1}{n}\sum_{i=1}^{n}(X_i - Y_i)^2 \tag{11}$$

$$\mathrm{RMSE} = \sqrt{\frac{1}{n}\sum_{i=1}^{n}(X_i - Y_i)^2} \tag{12}$$

## 5. Results and discussion

A computational fluid dynamics (CFD) analysis and Artificial Intelligence (AI) studies are combined to predict the mixed bioconvection flow of nanofluid of oxytactic bacteria through a porous cavity with inlet and outlet under periodic magnetic field. In the study, artificial intelligence prediction based on LightGBM algorithm was used. Fixed parameters are taken as $\epsilon = 0.8, Pr = 6.2, Da = 10^{-3}, \theta = 0, R_b = 10, \phi = 0.01, \zeta = \chi = 1, Ha = 25, Re = 100, Ri = 1, Le = 1, Pe = 1$, unless otherwise mentioned.

### 5.1. Effect of the Reynolds number ($Re$)

Effects of Reynolds number on streamlines, isotherms, oxygen concentration and motile are presented in Fig. 3. Some part of the flow goes almost diagonally from inlet port to outlet one and flow strength becomes very high at that ports. This is clear from streamlines Fig. 3(a). A circulation cell is formed at the top left corner and it becomes enlarged with increasing of Reynolds number values. On the contrary, there is no circulation cell at other corners due to lower values of Reynolds numbers. Isotherms are presented in Fig. 3(b). Increasing of Reynolds numbers does make any effect near walls. It is noticed that boundaries are heated under constant temperature and aim is to get cooler the inside of the cavity. Thus, cold air is penetrated inside the cavity with increasing of Reynolds number and both bottom side of diagonal of the cavity and right top corner becomes cooler. Both oxygen concentration and motile microorganisms density in Fig. 3(c) and (d) exhibit a similar distribution with temperature. Increasing of Reynolds number, these distributions are pushed to bottom side of the enclosure and right top side. On the contrary a wavy distribution is observed near the top left corner due to circulating of fluid at that part of the cavity with the effects of flow from inlet port.

Fig. 4(a)–(c) illustrated the variation of the average Nusselt number, average Sherwood numbers and average motile microorganism with Reynolds number. Results are presented for different values of nanoparticle volume fraction. As seen from the figure that all values are increased with increasing of Reynolds number which are expected

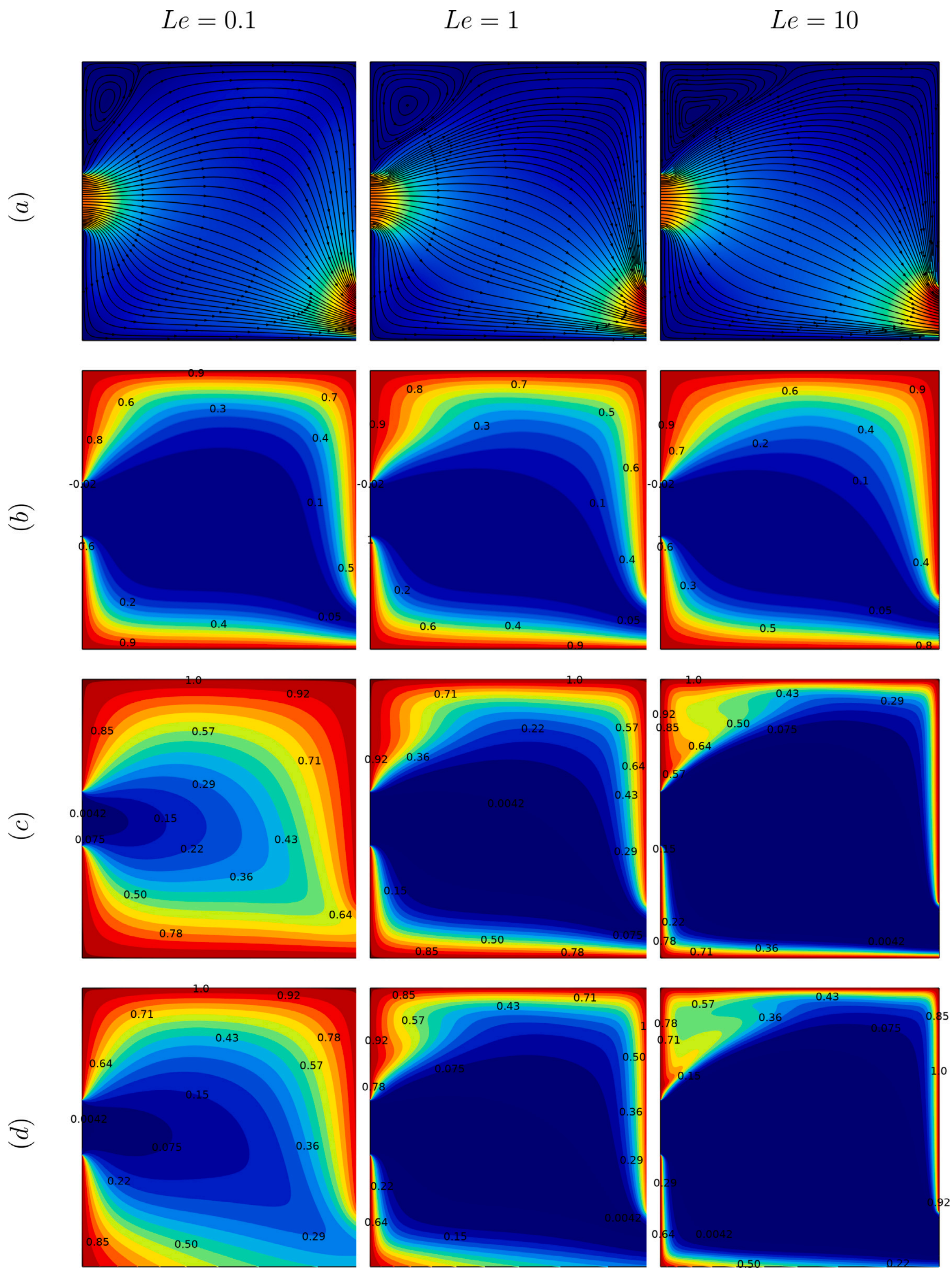


**Fig. 7.** The (a) streamlines, (b) temperature, (c) oxygen concentration, (d) motile microorganisms, for the variations of *Le*.

results due to increasing of kinetic energy of the fluid. Heat transfer exhibits an increment with addition of nanoparticles and these differences are increased with increasing of nanoparticle volume fraction and higher values of Reynolds number. On the contrary changing of nanoparticle volume fraction does not make any significant effects on average values due to very small amount of particle.

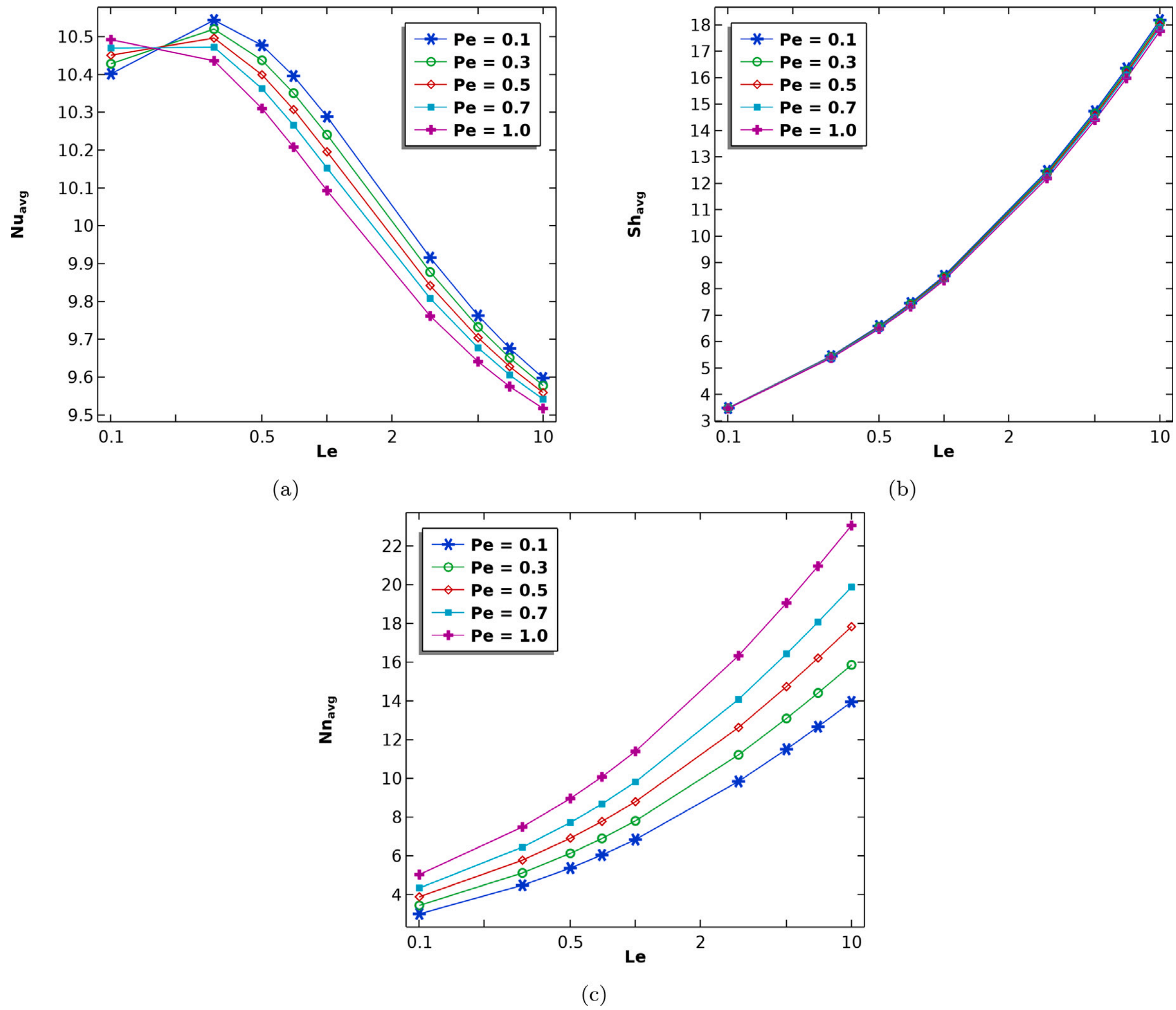


**Fig. 8.** The (a) average Nusselt number, (b) average Sherwood numbers and (c) average motile microorganism for the variation of $Pe$ as a function of $Le$.

### 5.2. Effect of the Richardson number ($Ri$)

Effects of Richardson number are presented on streamlines, isotherms, oxygen concentration and motile density are presented in Fig. 5(a) to (d). Richardson number is calculated for fixed Reynolds number by changing Grashof number. After inlet port and above and bottom side of inlet port behave as a separate cavity with increasing Richardson numbers. The flow at the left bottom corner stays almost motionless due to low velocity. When $Ri$ number is lower than 1, there is no circulation cell inside the cavity due to low $Re$ and low $Gr$ number effects even though forced convection heat transfer mode becomes dominant onto natural convection. For the highest value of $Ri$ number as in Fig. 5(d), convection heat transfer becomes dominant and plume like flow is occurred due to increasing of kinetic energy. Circulation cell is elongated under ceiling and streamlines are almost parallel to each other due to pushing flow through to upper side of the cavity. On the contrary of values of $Ri = 0.1$ and 1, S-shaped distribution is observed for oxygen concentration and motile microorganisms due to domination of natural convection heat transfer.

The changing of the average Nusselt number, average Sherwood numbers and average motile microorganism with Hartmann number at fixed parameters are presented. Effects of Richardson number are also presented in these figures. Thus, Fig. 6(a)–(c) shows the effects of magnetic field on the mixed convection system. As illustrated from the figure, all values are decreased linearly with increasing of Hartmann number due to decreasing of kinetic energy of the flow of the nanofluid. Increment between the values are decreased with decreasing of Richardson numbers. In other words, slope of the curve is lower for the lowest value of Richardson number. Higher values are obtained with increasing of Richardson numbers.

### 5.3. Effect of the Lewis number ($Le$)

Effects of Lewis number are presented in Fig. 7 via streamlines, isotherms, oxygen concentration, motile density ratio with $Le = 0.1$ (left column), $Le = 1$ (middle column) and $Le = 10$ (right column). As shown from the streamlines Fig. 7(a), circulation cell is observed at the left top corner and its strength is increased with increasing of $Le$ number. Lewis number becomes insignificant for flow field at the other parts of the cavity. Oxygen concentration is separated inside the cavity with increasing of Lewis number. Both trends and distribution of motile density resemble to oxygen distribution. Again, effects of Lewis number are given in Fig. 8(a)–(c) for average $Nu$ number, average Sherwood numbers and average motile microorganism with different Peclet number. Average Nusselt number values are decreased with increasing of $Le$ number. Average Nusselt number and Sherwood numbers show opposite behavior. There is an intersection point at $Le = 0.25$. For lower values of $Le$ number, higher results are observed with higher Peclet number due to higher kinetic energy. Lower values of Nusselt number is shown with increasing of Peclet numbers almost linearly. On the contrary, changing of Peclet number becomes insignificant on changing of average Sherwood number values. Motile microorganism values are

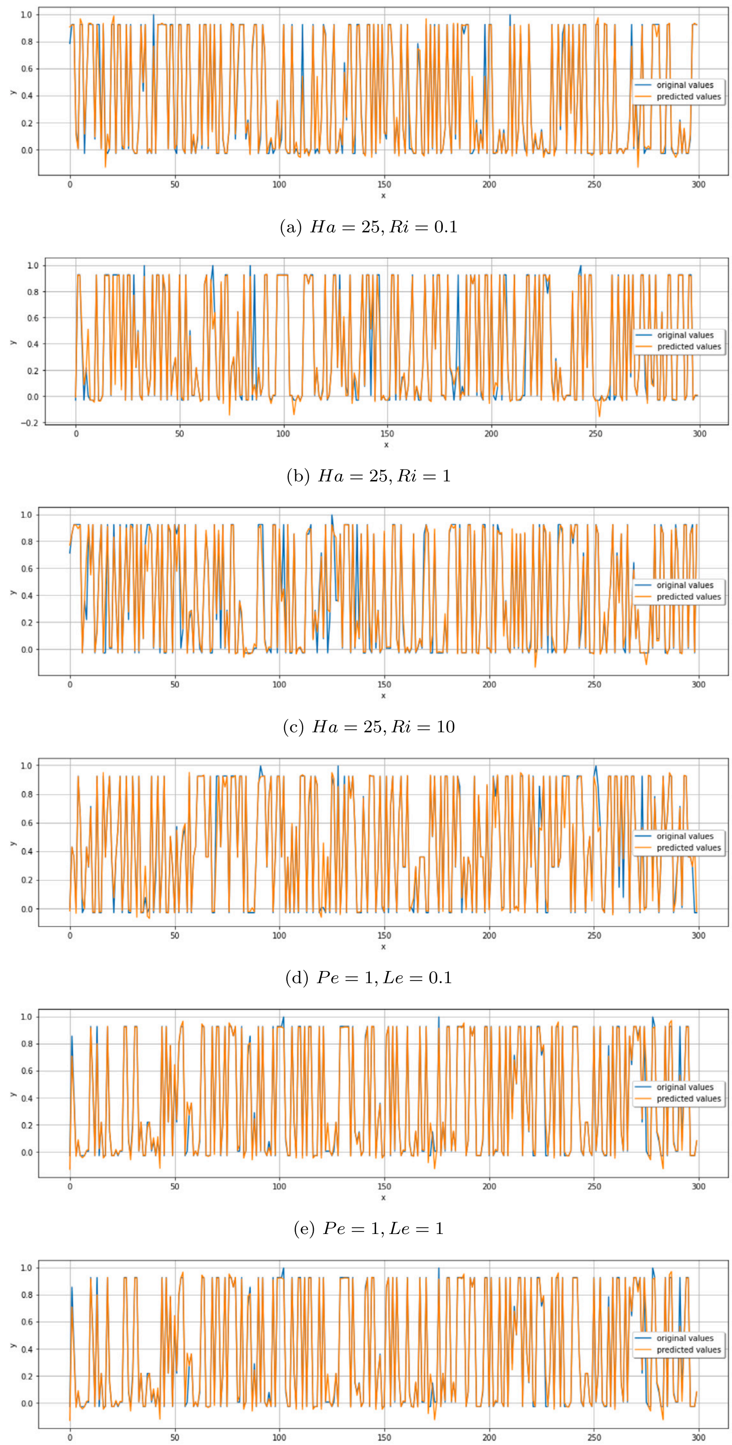


(a) $Ha = 25, Ri = 0.1$

(b) $Ha = 25, Ri = 1$

(c) $Ha = 25, Ri = 10$

(d) $Pe = 1, Le = 0.1$

(e) $Pe = 1, Le = 1$

(f) $Pe = 1, Le = 10$

**Fig. 9.** Prediction of $N$ values for various values of $Ri$ and $Le$.

increased with increasing of Peclet number and Lewis number almost linearly.

### 5.4. Artificial intelligence approach

For the study, a 70%/30% train–test split was employed, where 70% of each dataset was allocated for training and the remaining 30% was reserved for testing purposes. The estimation graphs in Figs. 1 to 3 depict the results obtained from 300 randomly selected data points out of the total 1000 data points used for testing. To prevent overfitting in the regression analysis using the LightGBM algorithm, the parameters were adjusted accordingly. Specifically, the "num_leaves" parameter was set to 10, controlling the complexity of the model. LightGBM is a gradient boosting framework used to perform regression analysis for this study. In general, it has two limitations: overfitting and inability to set the parameters correctly. In this study, to avoid overfitting, the data was randomly selected and the training–testing ratio was set to 70%–30%. The learning rate coefficient was chosen as 0.05, determining

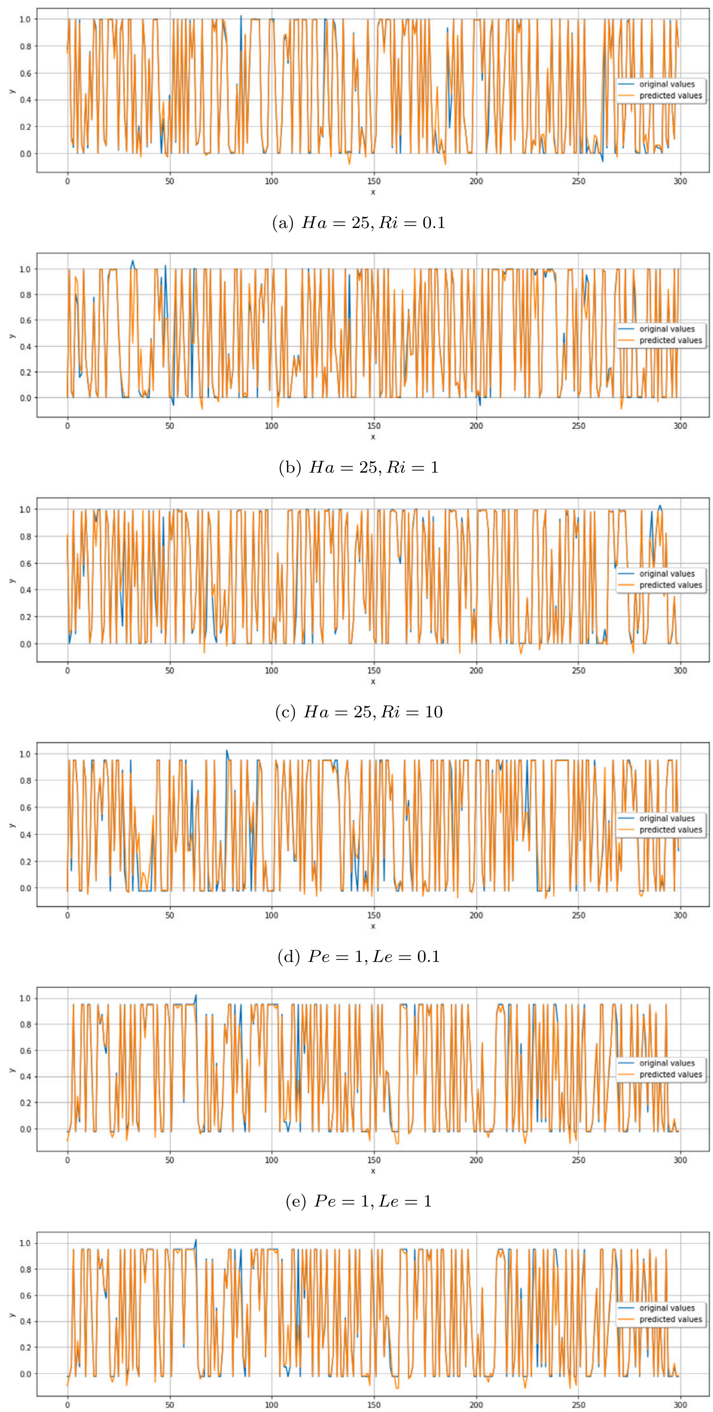


(a) $Ha = 25, Ri = 0.1$

(b) $Ha = 25, Ri = 1$

(c) $Ha = 25, Ri = 10$

(d) $Pe = 1, Le = 0.1$

(e) $Pe = 1, Le = 1$

(f) $Pe = 1, Le = 10$

**Fig. 10.** Prediction of $T$ values for various values of $Ri$ and $Le$.

the step size for updating the model during the training process. These parameter selections were made to achieve optimal performance and prevent overfitting in the regression analysis (see Figs. 9–11).

The performance comparison for 18 datasets obtained from the CFD study is given in Table 5. Upon examining the table, it is evident that the $R^2$ values for the datasets range between 95% and 98%, indicating a high level of accuracy in the estimation. Additionally, the MSE and RMSE values are observed to be low, further confirming the quality of the estimation. The study also includes the calculation of the mean of actual values (MAV) and the mean of predicted values (MPV). Table 5

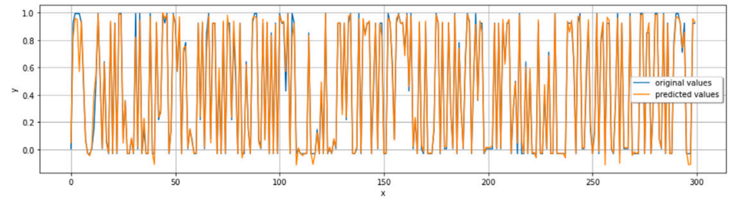


(a) $Ha = 25, Ri = 0.1$

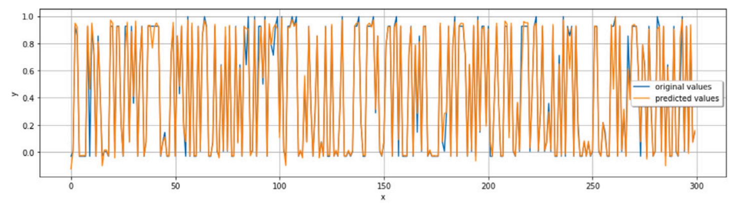


(b) $Ha = 25, Ri = 1$

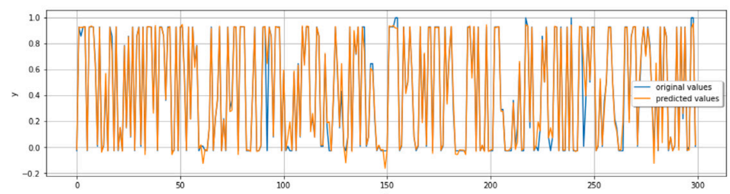


(c) $Ha = 25, Ri = 10$

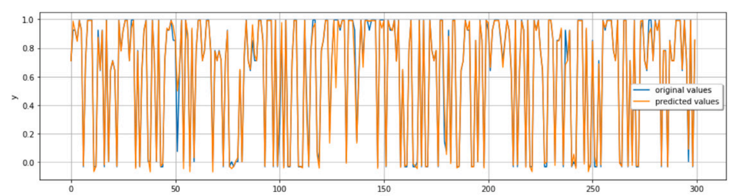


(d) $Pe = 1, Le = 0.1$

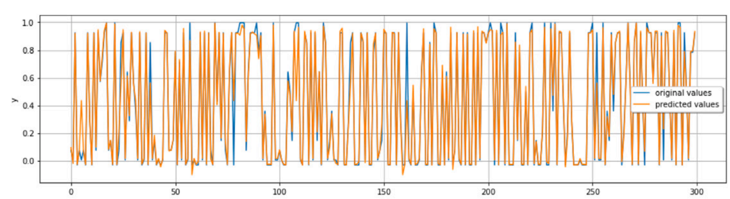


(e) $Pe = 1, Le = 1$

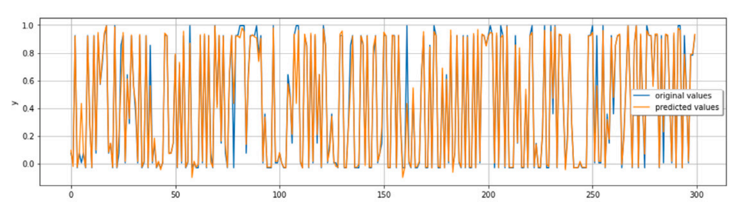


(f) $Pe = 1, Le = 10$

**Fig. 11.** Prediction of $\xi$ values for various values of $Ri$ and $Le$.

demonstrates that the MAV and MPV values obtained for each dataset exhibit close proximity to each other, signifying the success of the estimation process.

## 6. Conclusion

A computational fluid Dynamics analysis with artificial intelligence techniques are combined to obtain, flow field, temperature distribution, motile density and oxygen concentration for different chosen parameters under magnetic field. Following findings can be drawn as follows:

- Changing of Peclet number becomes insignificant on changing of average Sherwood number values. Motile microorganism values are increased with increasing of Peclet number and Lewis number almost linearly.
- Variation of Lewis number is more effective on oxygen concentration and motile density than that of flow field and temperature distribution.
- Magnetic field is a control parameter for all values and average values are decreased with increasing of magnetic field at different Richardson numbers. Differences among values are higher for higher values of Richardson numbers.

**Table 5**
Comparison of performance metrics for datasets.

| Dataset | $R^2$ | MSE | RMSE | MAV | MPV |
|---|---|---|---|---|---|
| $N(Ha = 25, Ri = 0.1)$ | 0.953579 | 0.009066 | 0.095213 | 0.392806 | 0.377627 |
| $N(Ha = 25, Ri = 1)$ | 0.966342 | 0.006039 | 0.077713 | 0.347000 | 0.342532 |
| $N(Ha = 25, Ri = 10)$ | 0.961526 | 0.006448 | 0.080298 | 0.346882 | 0.347661 |
| $N(Pe = 1, Le = 0.1)$ | 0.957644 | 0.006600 | 0.081239 | 0.468361 | 0.466218 |
| $N(Pe = 1, Le = 1)$ | 0.967608 | 0.006034 | 0.077678 | 0.384306 | 0.381386 |
| $N(Pe = 1, Le = 10))$ | 0.977946 | 0.004105 | 0.064069 | 0.323743 | 0.322002 |
| $T(Ha = 25, Ri = 0.1)$ | 0.969837 | 0.006034 | 0.077678 | 0.488977 | 0.488737 |
| $T(Ha = 25, Ri = 1)$ | 0.964258 | 0.007050 | 0.083963 | 0.531404 | 0.526254 |
| $T(Ha = 25, Ri = 10)$ | 0.976520 | 0.004522 | 0.067245 | 0.463537 | 0.464792 |
| $N(Pe = 1, Le = 0.1)$ | 0.970996 | 0.005633 | 0.075052 | 0.465750 | 0.468257 |
| $N(Pe = 1, Le = 1)$ | 0.963391 | 0.007027 | 0.083826 | 0.441875 | 0.444081 |
| $N(Pe = 1, Le = 10)$ | 0.967064 | 0.006234 | 0.078957 | 0.439375 | 0.446557 |
| $\xi(Ha = 25, Ri = 0.1)$ | 0.964466 | 0.007064 | 0.084050 | 0.428931 | 0.422243 |
| $\xi(Ha = 25, Ri = 0.1)$ | 0.967180 | 0.006489 | 0.080554 | 0.429639 | 0.425005 |
| $\xi(Ha = 25, Ri = 0.1)$ | 0.984753 | 0.002797 | 0.052889 | 0.439556 | 0.444969 |
| $\xi(Pe = 1, Le = 0.1)$ | 0.966710 | 0.005815 | 0.076255 | 0.642611 | 0.638855 |
| $\xi(Pe = 1, Le = 1)$ | 0.971579 | 0.005603 | 0.074853 | 0.441799 | 0.441733 |
| $\xi(Pe = 1, Le = 10)$ | 0.951798 | 0.009497 | 0.097455 | 0.344875 | 0.345358 |

- Addition of nanoparticle inside to the fluid becomes insignificant because heat and mass transfer and motile distribution do not affected with increasing of nanoparticle volume fraction.
- For this study, the LightGBM algorithm was employed for regression analysis. LightGBM is a relatively new algorithm known for its speed, efficiency, and high prediction performance. The comparison of performance metrics obtained in this study demonstrates that successful estimations, ranging from 95% to 98%, were achieved across all datasets. These findings highlight that artificial intelligence-based estimation algorithms, particularly for datasets obtained from Computational Fluid Dynamics (CFD) studies, can yield high accuracy and reliable results.

As a future work, second law analysis of thermodynamics will be studied and added to work.

## CRediT authorship contribution statement

**Shafqat Hussain:** Writing – original draft, Visualization, Validation, Software, Methodology, Investigation, Formal analysis, Conceptualization. **Hakan F. Öztop:** Writing – review & editing, Writing – original draft, Conceptualization. **Abdullah Madhi Alsharif:** Writing – original draft, Visualization, Formal analysis. **Fatih Ertam:** Writing – original draft, Visualization, Formal analysis.

## Declaration of competing interest

The authors declare that they have no known competing financial interests or personal relationships that could have appeared to influence the work reported in this paper.

## Data availability

Data will be made available on request.

## Acknowledgment

Abdullah Alsharif would like to thank Taif University, Saudi Arabia, for supporting this work through project number (TU-DSPP-2024-185).

## References

[1] A. Bisht, S. Maheshwari, Thermo-bioconvection in nanoliquid suspension saturated with thermotactic microorganisms, Forces Mech. 9 (2022) 100128.
[2] S. Hussain, B.P. Geridonmez, Mixed bioconvection flow of Ag-MgO/water in the presence of oxytactic bacteria and inclined periodic magnetic field, Int. Commun. Heat Mass Transfer 134 (2022) 106015.
[3] M. Ferdows, K. Zaimi, A.M. Rashad, H.A. Nabwey, MHD bioconvection flow and heat transfer of nanofluid through an exponentially stretchable sheet, Symmetry 12 (5) (2020).
[4] J.R. Platt, "Bioconvection patterns" in cultures of free-swimming organisms, Science 133 (3466) (1961) 1766–1767.
[5] T.J. Pedley, N.A. Hill, J.O. Kessler, The growth of bioconvection patterns in a uniform suspension of gyrotactic micro-organisms, J. Fluid Mech. 195 (1988) 223–237.
[6] T.J. Pedley, J.O. Kessler, Hydrodynamic phenomena in suspensions of swimming microorganisms, Annu. Rev. Fluid Mech. 24 (1) (1992) 313–358.
[7] N. Hill, T. Pedley, Bioconvection, Fluid Dyn. Res. 37 (1) (2005) 1–20, Biofluiddynamics.
[8] M.A. Sheremet, I. Pop, Thermo-bioconvection in a square porous cavity filled by oxytactic microorganisms, Transp. Porous Media 103 (2014) 191–205.
[9] S.U. Choi, J.A. Eastman, Enhancing thermal conductivity of fluids with nanoparticles, in: ASME International Mechanical Engineering Congress & Exposition, 1995.
[10] A. Kuznetsov, Bio-thermal convection induced by two different species of microorganisms, Int. Commun. Heat Mass Transfer 38 (5) (2011) 548–553.
[11] M. Sheremet, T. Grosan, I. Pop, MHD free convection flow in an inclined square cavity filled with both nanofluids and gyrotactic microorganisms, Internat. J. Numer. Methods Heat Fluid Flow 29 (2019) 4642–4659.
[12] D.K. Mandal, N. Biswas, N.K. Manna, R.S.R. Gorla, A.J. Chamkha, Role of surface undulation during mixed bioconvective nanofluid flow in porous media in presence of oxytactic bacteria and magnetic fields, Int. J. Mech. Sci. 211 (2021) 106778.
[13] S. Hussain, A.M. Aly, H.F. Öztop, Magneto-bioconvection flow of hybrid nanofluid in the presence of oxytactic bacteria in a lid-driven cavity with a streamlined obstacle, Int. Commun. Heat Mass Transfer 134 (2022) 106029.
[14] F. Selimefendigil, H.F. Öztop, CFD analysis and optimization of nano-enhanced phase change process in multiple port vented cavity equipped with encapsulated PCM under the combined effects of triple rotating cylinders and inclined magnetic field, J. Magn. Magn. Mater. 575 (2023) 170716.
[15] A. Aghaei, S. Bhattacharyya, A. Dezfulizadeh, A. Goldanlou, S. Rostami, M. Sharifpur, Heat transfer and fluid flow analysis using nanofluids in diamond-shaped cavities with novel obstacles, Eng. Appl. Comput. Fluid Mech. 15 (1) (2021) 1034–1056.
[16] L.M. Jasim, H. Hamzah, C. Canpolat, B. Sahin, Mixed convection flow of hybrid nanofluid through a vented enclosure with an inner rotating cylinder, Int. Commun. Heat Mass Transfer 121 (2021) 105086.
[17] C.S. Balla, C. Haritha, K. Naikoti, A. Rashad, Bioconvection in nanofluid-saturated porous square cavity containing oxytactic microorganisms, Internat. J. Numer. Methods Heat Fluid Flow (2018) HFF–05–2018–0238.
[18] S. Hussain, F. Ertam, M.B.B. Hamida, H.F. Oztop, N.H. Abu-Hamdeh, Analysis of bioconvection and oxytactic microorganisms in a porous cavity with nano-enhanced phase change materials and quadrant heater: Application of support vector regression based model, J. Energy Storage 63 (2023) 107059.
[19] S. Hussain, F. Ertam, M.B. Ben Hamida, H.F. Oztop, N.H. Abu-Hamdeh, Passive control of, energy storage of NePCM, heat and mass transfer with gamma-shaped baffle in a thermo-bioconvection system using CFD and artificial intelligence, Int. Commun. Heat Mass Transfer 144 (2023) 106764.
[20] J.H. Friedman, Greedy function approximation: A gradient boosting machine, Ann. Statist. 29 (5) (2001) 1189–1232.
[21] T. Chen, C. Guestrin, XGBoost: A scalable tree boosting system, in: Proceedings of the 22nd ACM SIGKDD International Conference on Knowledge Discovery and Data Mining, KDD '16, Association for Computing Machinery, New York, NY, USA, 2016, pp. 785–794.
[22] J. Lin, W. Lin, W. Lin, J. Wang, H. Jiang, Thermal prediction for Air-cooled data center using data Driven-based model, Appl. Therm. Eng. 217 (2022) 119207.
[23] S. Yao, A. Kronenburg, A. Shamooni, O. Stein, W. Zhang, Gradient boosted decision trees for combustion chemistry integration, Appl. Energy Combust. Sci. 11 (2022) 100077.
[24] M.A. Qureshi, S. Hussain, M.A. Sadiq, Numerical simulations of MHD mixed convection of hybrid nanofluid flow in a horizontal channel with cavity: Impact on heat transfer and hydrodynamic forces, Case Stud. Therm. Eng. 27 (2021) 101321.
[25] M. Izadi, M.A. Sheremet, S. Mehryan, Natural convection of a hybrid nanofluid affected by an inclined periodic magnetic field within a porous medium, Chinese J. Phys. 65 (2020) 447–458.
[26] S. Saeidi, J. Khodadadi, Transient flow and heat transfer leading to periodic state in a cavity with inlet and outlet ports due to incoming flow oscillation, Int. J. Heat Mass Transfer 50 (3) (2007) 530–538.
[27] S. Hussain, F. Schieweck, S. Turek, Efficient Newton-multigrid solution techniques for higher order space–time Galerkin discretizations of incompressible flow, Appl. Numer. Math. 83 (2014) 51–71.

[28] S. Hussain, K. Mehmood, M. Sagheer, A. Farooq, Entropy generation analysis of mixed convective flow in an inclined channel with cavity with $Al_2O_3$-water nanofluid in porous medium, Int. Commun. Heat Mass Transfer 89 (2017) 198–210.
[29] S. Hussain, S. Shoeibi, T. Armaghani, Impact of magnetic field and entropy generation of Casson fluid on double diffusive natural convection in staggered cavity, Int. Commun. Heat Mass Transfer 127 (2021) 105520.
[30] N.S. Gibanov, M.A. Sheremet, M.A. Ismael, A.J. Chamkha, Mixed convection in a ventilated cavity filled with a triangular porous layer, Transp. Porous Media (2017) 1–21.
[31] G. Ke, Q. Meng, T. Finley, T. Wang, W. Chen, W. Ma, Q. Ye, T.-Y. Liu, LightGBM: A highly efficient gradient boosting decision tree, in: I. Guyon, U.V. Luxburg, S. Bengio, H. Wallach, R. Fergus, S. Vishwanathan, R. Garnett (Eds.), Advances in Neural Information Processing Systems, Vol. 30, Curran Associates, Inc., 2017.
[32] X. Sun, M. Liu, Z. Sima, A novel cryptocurrency price trend forecasting model based on LightGBM, Finance Res. Lett. 32 (2020) 101084.
[33] D. Chicco, M.J. Warrens, G. Jurman, The coefficient of determination R-squared is more informative than SMAPE, MAE, MAPE, MSE and RMSE in regression analysis evaluation, PeerJ Comput. Sci. 7 (2021) e623.